Three-Dimensional Blade and Hub Stresses of Coaxial Rotors in Forward Flight

Mrinalgouda Patil*
Post-Doctoral Associate

Anubhav Datta
Associate Professor

University of Maryland, College Park, MD

A three-dimensional (3D) solid finite element analysis model is developed to predict blade and hub stresses of a lift-offset coaxial rotor in forward flight. The model is open source, with a generic internal structure, but with rotor radius, planform, number of blades, hub type, and rotor frequencies loosely resembling a modern lift-offset coaxial rotor. Comprehensive analysis is carried out with a lifting-line aerodynamic model with free wake. Two steady-level flight regimes are considered: a low-speed transition ($\mu = 0.1$) and a high-speed cruise regime ($\mu = 0.35$). Two typical lift-offsets are considered: zero ($LO = 0$) and 10% of rotor radius ($LO = 0.1$). Two blade models are considered: a high flap frequency ($\nu_\beta = 1.44$/rev) and a low flap frequency model ($\nu_\beta = 1.23$/rev). The predicted airloads are verified qualitatively with recently published industry predictions. The predicted stresses are unique to this paper. Their 3D nature is revealed by this analysis. Predictions indicate that lowering the frequency of the first flap mode while tailoring the shape of the second flap mode might help relieve stresses significantly (50%) while also avoiding the danger of blade strike at high speed. Even though specific conclusions are premature without the exact properties of an actual aircraft and a higher fidelity aerodynamic model, it appears clear that blade flexibility may be a key factor even for these stiff rotors to relieve blade and hub stresses.

Nomenclature

C_{M_X}	hub roll moment $\div \rho A (\Omega R)^2 R$
C_Q	torque $\div \rho A (\Omega R)^2 R$
C_T	thrust $\div \rho A (\Omega R)^2$
D	rotor diameter, ft (m)
LO	lift-offset, % R
M_X	hub roll moment, ft-lbf (N-m)
N_b	number of blades
R	rotor radius, ft (m)
r	radial location, ft (m)
z	interrotor spacing, ft (m)
α	shaft tilt angle, deg
β_p	pre-cone, deg
θ	blade pitch angle
θ_{75}	collective
θ_{1c}	lateral cyclic
θ_{1s}	longitudinal cyclic
μ	tip speed $\div \Omega R$
σ	rotor solidity
σ_{11}	axial stress, lbf/in^2 (N/m^2)
ψ	blade azimuth angle
Ω	rotor rotation speed, rad/s

Introduction

A three-dimensional (3D) solid finite element analysis (FEA) model is developed to demonstrate the prediction of blade and hub stresses of a lift-offset coaxial rotor. The structural model is a departure from the current state-of-the-art comprehensive codes, where one-dimensional (1D) beam-based models are used for the rotor. The aerodynamic model is typical of current state-of-the-art—a low-fidelity unsteady lifting-line model with two-dimensional airfoil tables and free-wake. The trim controls are typical of a lift-offset coaxial rotor.

The University of Maryland/U.S. Army software—X3D (Refs. 2, 3) is the analysis platform through which 3D structures are introduced. An example of a 3D structural model of a coaxial rotor was presented by the authors in Refs. 4–6. That model was called Metaltail. This paper advances the earlier model. The new model is inspired by the Sikorsky S-97 Raider® in gross dimensions, and geometry is available in the public domain. The new model is called Metaltail-II. The hub remains similar to the earlier model. The blade twist and internal structure resemble a modern rotor but are generic. The geometry is tailored somewhat to produce rotating frequencies typical of a lift-offset rotor. It is expected that this model will generate representative blade loads—steady and vibratory—which a modern coaxial hub must absorb to
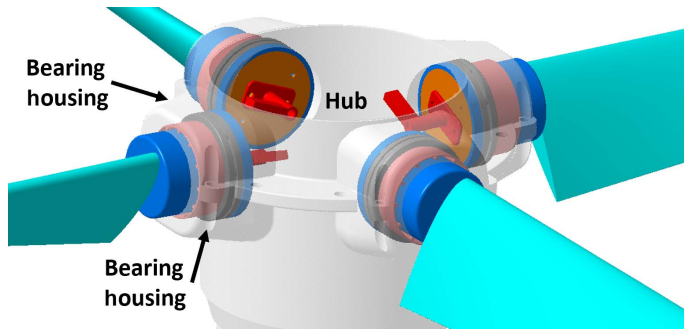
Fig. 1. CATIA model of the upper rotor hub.

enable its promise of higher speeds far beyond a classical single main rotor helicopter.

Background and motivation

Achieving high speeds without compromising hover efficiency has been an enduring quest for rotary-wing aircraft. In forward flight, the high-speed performance of a single main rotor helicopter is limited by compressibility on the advancing blade and reverse flow and dynamic stall on the retreating blade. As a result, the lift capability depletes on the retreating blade which forces the advancing blade to sacrifice its lift to achieve zero roll moment. A hingeless coaxial allows its advancing blades to continue providing lift to full potential and uses the opposite turning rotors to cancel the roll moments appearing at the individual hubs. This provides substantial benefits in speed, but the price paid is the high-roll moments at the individual hubs. These must be absorbed either by more structure or by greater blade flapping.

The individual hub roll moments are quantified by a nondimensional parameter called the lift-offset (*LO*). It represents the lateral offset of the net lift as a fraction of the radius (Ref. 7) and is defined as

$$LO = \frac{|M_X^U| + |M_X^L|}{(T^U + T^L)R} = \frac{|C_{M_X}^U| + |C_{M_X}^L|}{C_T^U + C_T^L}. \tag{1}$$

The variables $|M_X^U|$ and $|M_X^L|$ are the absolute values of the individual hub roll moments of the upper and lower rotors, respectively, and T^U and T^L are the corresponding thrusts. The moments are added because the total thrust is in the denominator, and the absolute values are taken because that gives the net moment on the shaft connecting the two rotors even though they cancel before reaching the aircraft. When $LO = 0$, the net lift acts at the center of the hub, and the shaft experiences minimum bending moment. An articulated hub could also allow its advancing blades to lift freely and absorb the moments naturally with a flap hinge. This is the implementation in Kamov coaxial helicopters. The penalty would be high blade flapping which at high speeds would make blade strike inevitable. Thus, the fundamental trade-off in a coaxial design is high hub loads versus rotor spacing. Lift-offset coaxial helicopters absorb high loads with stiff hingeless hubs instead of a flapping hinge. This prevents blade strike with minimum interrotor spacing consistent with the need for a low drag hub for high-speed flight. However, absorbing high loads within allowable stresses requires a heavy hub, which impacts the entire aircraft from the hub down. To maximize the full potential of the lift-offset coaxial, hub stresses must be better understood, reliably predicted, and ultimately absorbed with minimum weight. These are the overall objectives of this research.

The modern lift-offset concept was first introduced in the United States by the Sikorsky XH-59A demonstrator aircraft during the 1970s (Ref. 8). The technology was significantly advanced in the 2000s by the X2-Technology Demonstrator (Refs. 9–12), which ultimately led to the
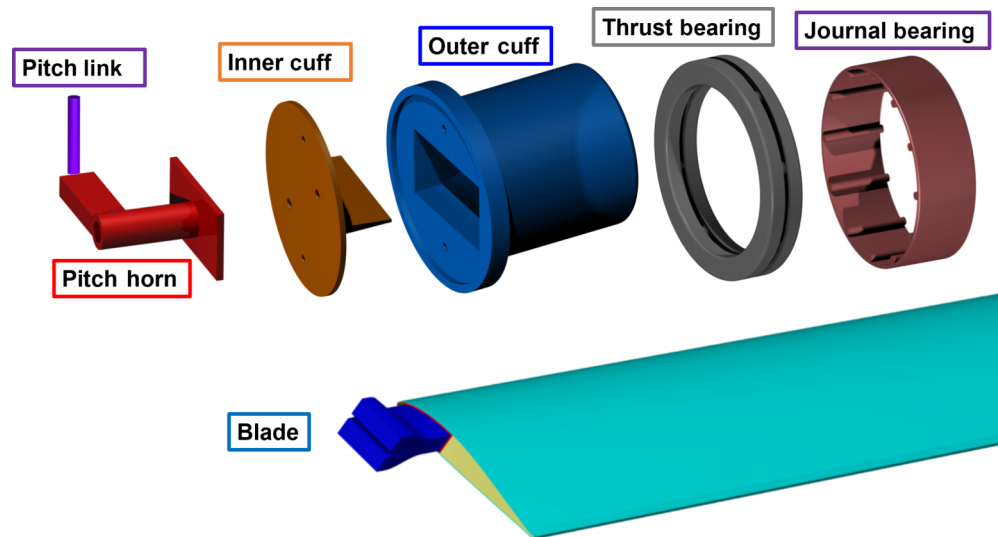

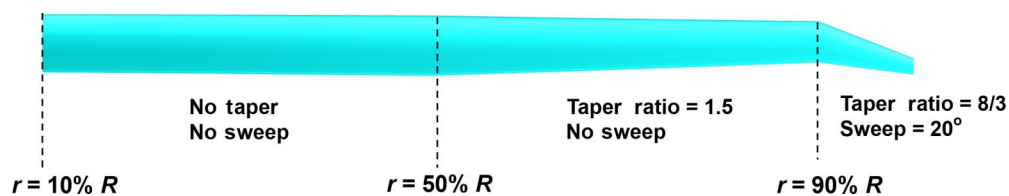**Fig. 2. CATIA models of an individual blade and its parts.**

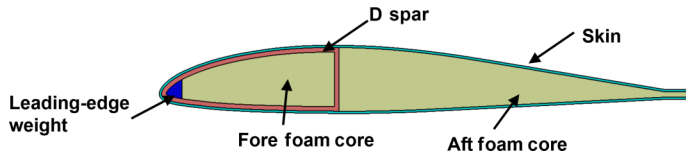**Fig. 3. Blade planform depicting the taper and sweep along the span.**

Fig. 4. CAD model of the blade cross-section at the root; VR-7 airfoil.

Table 1. Properties of the Metaltail-II rotor

Property	Value
Radius, R	5.18 m (17 ft)
Number of blades, N_b	4
Precone, β_p	1.5°
Solidity, σ	0.0636
Rotor separation, z/D	0.07
Rotor speed, Ω	410 RPM (43 rad/s)

development of the larger S-97 Raider® and Sikorsky-Boeing SB>1 aircraft. Together with the modern tiltrotors, these aircraft seek to expand cutting-edge high-speed helicopter technology. Thus the coaxial rotor remains an interesting and important area of research. There has been a considerable amount of research on coaxial rotors. The review by Coleman surveys work in the United States and the former Soviet Union and Russia up to 1997 (Ref. 13). Research in the 21st century has been driven by Sikorsky tests (Ref. 14) and analysis (Refs. 15, 16), U.S. government studies (Refs. 7, 17, 18), including small-scale hover tests (Refs. 19, 20), and basic research investigations at the University of Maryland (Refs. 21, 22), University of Texas at Austin (Refs. 23, 24), and other academia (Refs. 25–27). Typically, the industry focused on new aircraft development, the government provided design explorations for capability expansion, and academia filled fundamental gaps in knowledge and tools.

A key limitation of all state-of-the-art tools has been 1D beam-based structural models of the rotor. These types of models are incapable of predicting 3D stresses in all parts of the rotor especially the hub parts where 3D modeling is critical. The objective of this paper is to advance the state-of-the-art to 3D models. 3D modeling was identified as a key requirement for next-generation rotorcraft comprehensive analysis by NASA in 2008 (Ref. 28). This directly led to the development of the University of Maryland/U.S. Army aeroelastic solver X3D. The first version in 2016 was serial software. Since then, the development of massively parallel and scalable solvers (Refs. 2, 29, 30) has opened the opportunity to model larger and more complex problems. The emergence of digital thread in the form of sophisticated Computer-aided design (CAD) and meshing tools, and the explosion of computer power in the form of parallel computing architecture means such models can now be effectively built and efficiently computed in X3D. The objective of this paper is to demonstrate this task on the modern coaxial rotor.

The model developed in this paper—Metaltail-II—is intended to be a demonstration test case for inclusion in the U.S. Army/DOD rotorcraft simulation software CREATE™–AV Helios (Refs. 31, 32). Previously, a tiltrotor test case—TRAM—a 1/4-scale model of the V-22 was developed and executed within Helios (Ref. 33). The coaxial is intended to expand the test suite to cover the other major high-speed configuration. Execution within Helios will ultimately couple the

present analysis with a high-fidelity Reynolds-Averaged Navier-Stokes (RANS) CFD solver in addition to its internal lifting-line aerodynamic model.

Organization of paper

Following this introduction, the paper begins with a description of the geometry and 3D structural model of Metaltail-II. The next section carries out an analysis at low-speed transition flight. The low-speed flight allows predicted airloads to be verified with S-97 predictions recently published by Sikorsky (Refs. 15, 16). The Sikorsky predictions were carried out with high-fidelity RANS for aerodynamics, which, in the absence of test data, is deemed to be the next best basis for assessment. The following section carries out an analysis at high-speed cruise flight. Blade airloads and stresses are studied. The stresses are analyzed for two lift-offset conditions. The effect of blade flexibility is investigated. Finally, some key conclusions are drawn.

Metaltail-II

Metaltail-II is a notional coaxial rotor designed as an open-source test case for the U.S. Army/DOD rotorcraft simulation software CREATE™–AV Helios. The design is inspired by published gross dimensions of the Sikorsky S-97 Raider® but is otherwise entirely generic. Table lists the important rotor parameters.

The model shares similarities with the S-97 Raider® such as the hingeless hub, four blades per rotor, same rotor radius, similar blade planform, and similar interrotor spacing. The twist was set to −16 deg linear, nominally an approximation of the UH-60A Black Hawk. The hub is notional but has enough complexity to be suitable for a test case. The cross section was selected to be a VR-7 profile with a D-spar and carbon-fiber weaves to be sufficiently representative of a modern rotor. It is also a validated section; these sections have been fabricated and tested on Mach-scale rotors at the University of Maryland and validated in X3D recently (Ref. 34).
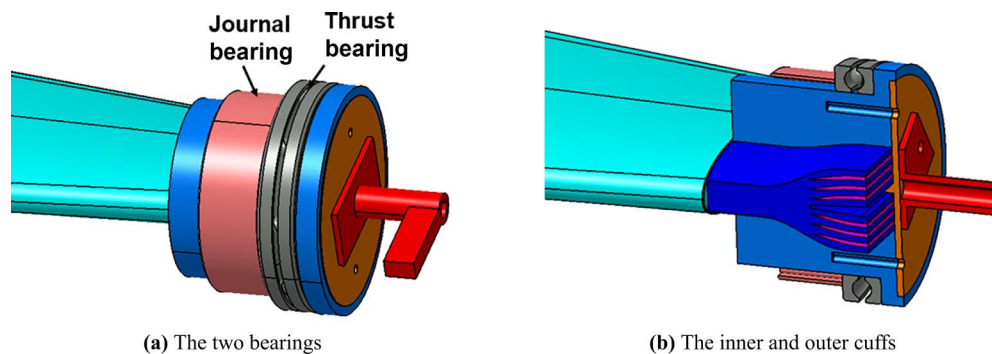

(a) The two bearings

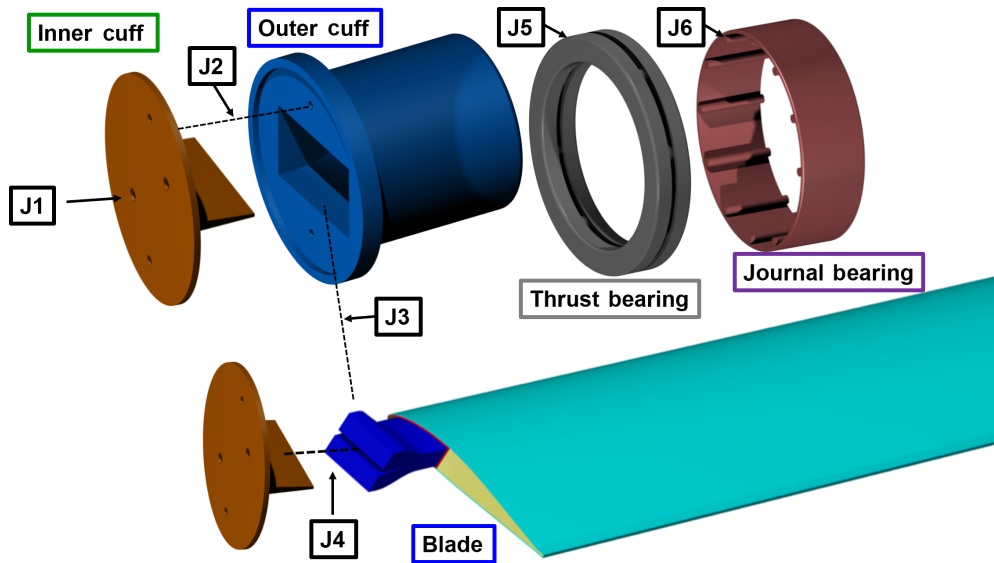(b) The inner and outer cuffs

Fig. 5. Parts of the blade root.

Fig. 6. The six joints on a blade.
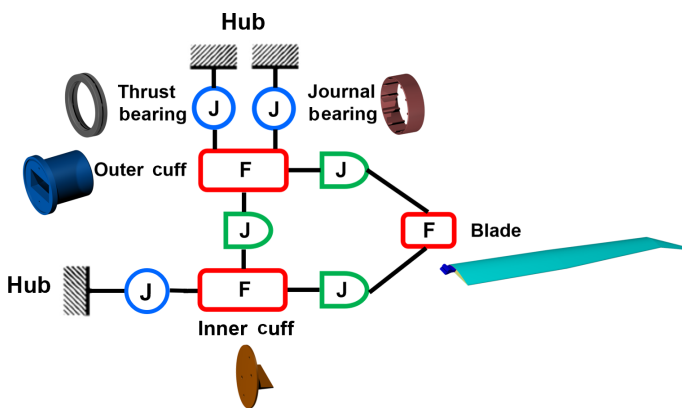
Fig. 7. Load flow diagram of Metaltail-II from blade to hub.

Fig. 8. 3D structural mesh of (a) single blade and (b) coaxial rotor.

CAD model

The first step in 3D modeling is to develop a CAD model. CATIA V5 is used. Figure 1 shows the CAD model for the upper rotor depicting attachment of the blades to the hub through the bearing housing. The blade root joins the individual parts—the blade, pitch horn, pitch link, outer cuff, inner cuff, thrust bearing, and journal bearing. Figure 2 shows the CAD model of each part separately. The connectivity between these parts is described later. The blade description consists of a surface profile (needed for aerodynamics) and a detailed internal structure (needed for dynamics).

Blade planform and cross section

Figure 3 shows the blade planform. The span is divided into three parts: (1) from 10% R to 50% R with no taper or sweep, (2) from 50% R to 90% R with a taper ratio of 1.5 but no sweep, and (3) from 90% R to tip with a taper ratio of 2.66 and back sweep of $20°$.

The section profile is VR-7. The internal structure consists of a tungsten leading edge weight, a solid uniaxial carbon-fiber D-spar, a machin-
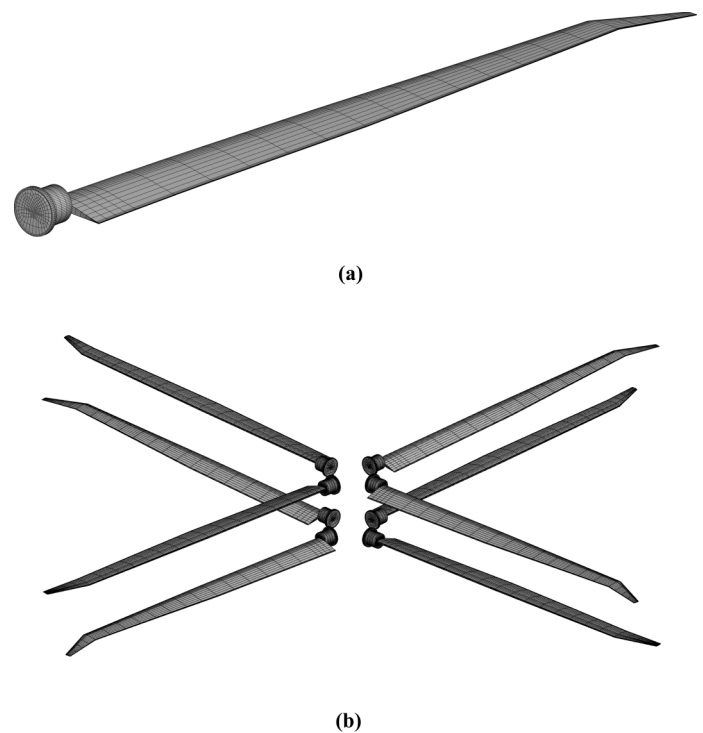
able foam aft core, and a uniaxial carbon fiber trailing edge block, all wrapped in a $\pm45°$ carbon fiber skin. This is shown in Fig. 4.

Structural analysis representation

The structural analysis representation assigns parts that are to be modeled using 3D finite elements (parts with strains) and parts that are to be relegated to joints (parts that are rigid). It defines the type and geometry of joints, makes joint connections, and assigns joint properties. The model has five flexible parts: the blade, pitch horn, pitch link, inner cuff, and outer cuff. The bearings, fittings between the flexible parts, and hub
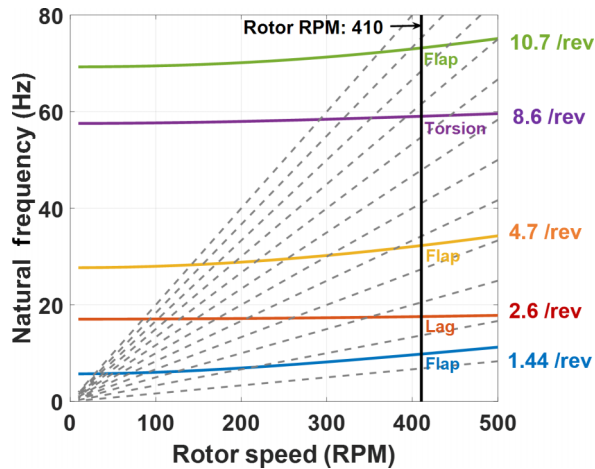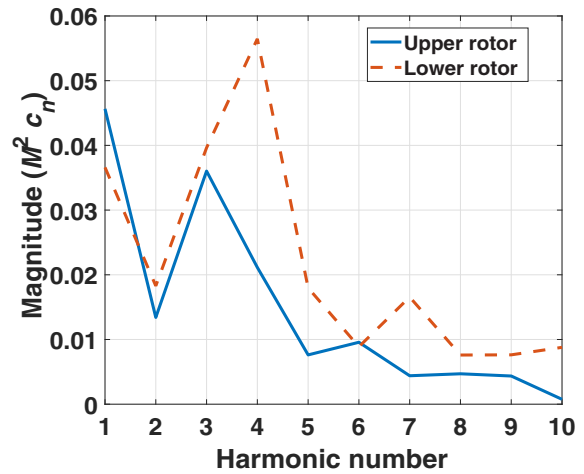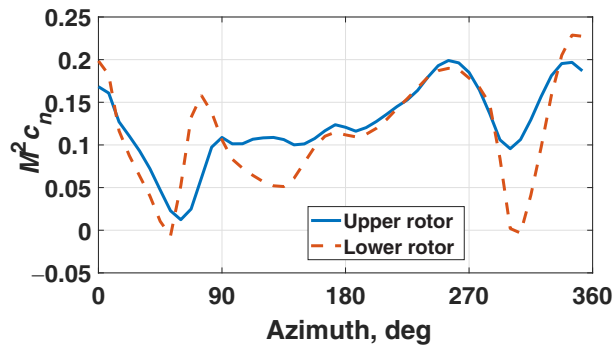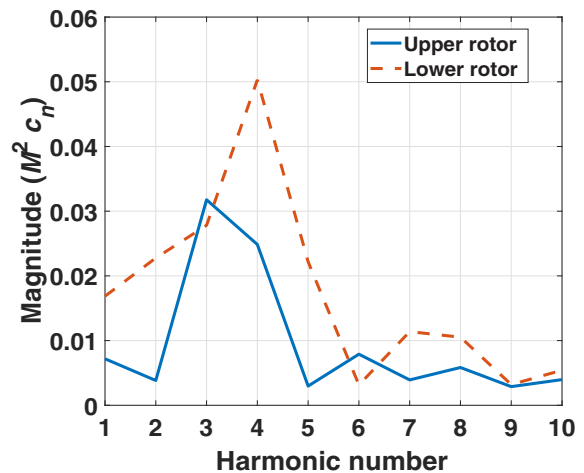
Fig. 9. Rotating frequencies for the Metaltail-II rotor blade.

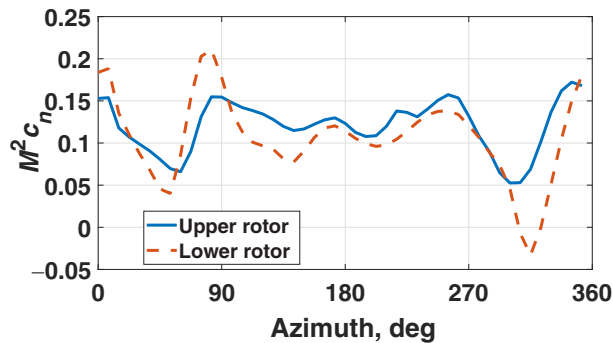(a) $LO = 0$

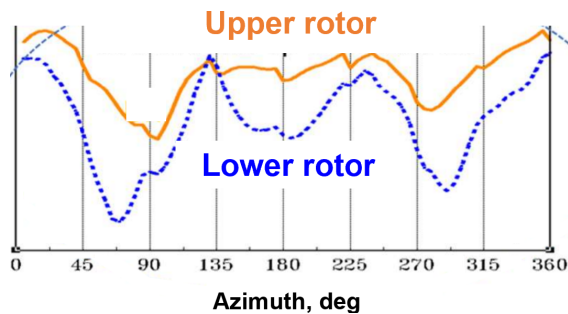(b) $LO = 0.1$

(c) $LO = 0$

Fig. 10. Predicted normal force versus azimuth for Metaltaill-II at 90% R in low-speed transition flight $\mu = 0.1$ for (a) $LO = 0$, (b) $LO = 0.1$; (c) Sikorsky predicted S-97 blade airloads near tip in low-speed transition flight 15.

(a) $LO = 0$

(b) $LO = 0.1$

Fig. 11. Predicted normal force harmonics at 90% R: low-speed transition $\mu = 0.1$.

connections are modeled as joints. Figure 1 shows how the blade root attaches to the hub. The blade root is sandwiched by the bearing housing from the top and bottom, which connects the thrust and journal bearing to the hub. The pitch horn is assembled at the root of each inner sleeve and connected to the upper swashplate with a pitch link (not shown in Fig. 1).

The bolts between the inner and outer cuffs, thrust and journal bearings, and pitch link connections to the pitch horn and the hub are all modeled as joints. The exposed root of the blade mates into the inner surfaces of the outer cuff, and the inner cuff locks into the open slot of the blade as shown in Fig. 5(b), so the connections between the blade and both the cuffs can be modeled as rigid joints. The outer cuff is connected to the rotor hub through two bearings, as shown in Fig. 5(a). The thrust bearing transfers only the axial force to the hub. The journal bearing transfers thrust, in- and out-of-plane shears, and the flap and lead-lag moments. The inner cuff is connected to a pitch horn, which is then connected to a pitch link on the leading edge side of the blade. The torsion moment is transferred through the inner cuff to the pitch link, which carries it to the hub. The pitch horn and pitch link can be neglected during meshing; a root joint is sufficient for providing control inputs.
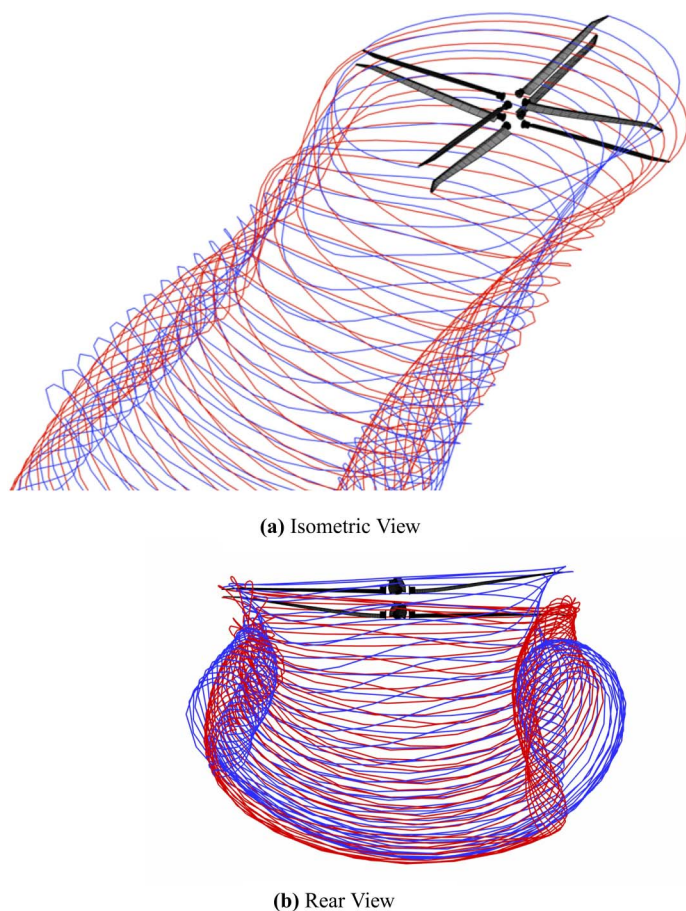
(a) Isometric View

(b) Rear View

Fig. 12. Free wake geometry at low-speed transition: $\mu = 0.1$, $LO = 0.1$.

Table 2. List of parts of Metaltail-II; connections with −1 indicate boundaries

Part No.	Flexible/. /Joint No.	Name	Type	Connections
P1	J1	jRoot	Joint	−1, P2
P2	F1	Inner Cuff	Flex	P1, P3, P7
P3	J2	jIcuffOcuff	Joint	P2, P4
P4	F2	Outer Cuff	Flex	P3, P6, P8, P9
P5	F3	Blade	Flex	P6, P7
P6	J3	jOcuffBlade	Joint	P4, P5
P7	J4	jIcuffBlade	Joint	P2, P5
P8	J5	jThrustBearing	Joint	−1, P4
P9	J6	jJournalBearing	Joint	−1, P4

(a) $LO = 0$

(b) $LO = 0.1$

Fig. 13. Axial stresses at low speed: $\mu = 0.1$, $C_T/\sigma = 0.08$, $\alpha_s = -2°$.

(a) $LO = 0$

(b) $LO = 0.1$

Fig. 14. Rear-side view of the coaxial rotor blades at low-speed flight with (a) $LO = 0$ and (b) $LO = 0.1$.

commanded to the joint (P1/J1) provide pitch control for the trim solution. Figure 7 shows the load flow diagram.

The hub is assumed rigid, so the upper and lower rotors are structurally independent. A single blade is modeled in each rotor. This is sufficient for the periodic trim solution. The assumption is that the blades are identical.

Structural analysis model

Once the part types are assigned, the individual flexible parts are meshed in Cubit to produce 27-noded isoparametric hexahedral brick elements. Part meshes are independent. The meshes and joints are assembled to create the final structural analysis model of the blade as shown in Fig. 8(a). The blades for both rotors are meshed and assembled together as shown in Fig. 8(b). Each rotor consists of 1920 bricks with a total of 55,000 degrees of freedom, so the full model consists of twice these numbers.

The final model has nine parts, three of which are flexible (5 minus the pitch horn and link) and six are joints. These are shown in Fig. 6 and listed in Table 2. Each part has two identifiers (ID), a part number (P#), and a type identifier (F# for flexible and J# for joint). The three flexible parts are meshed using brick finite elements. The six joint parts are assigned kinematic constraints using Euler angles. The three joints that are connected to the hub also serve as load sensors for root loads. These rotating frame loads are transformed into fixed frames for hub loads. The identifier −1 sets zero displacement boundary condition (in the rotating frame). Here, it is the hub—defined as the center of rotation. Rotations
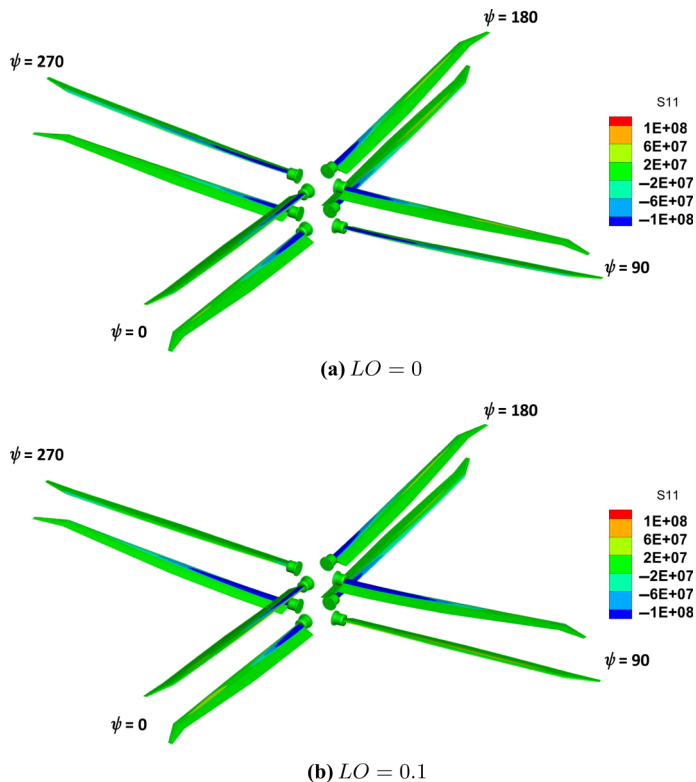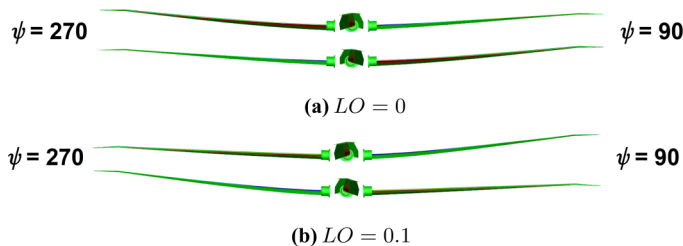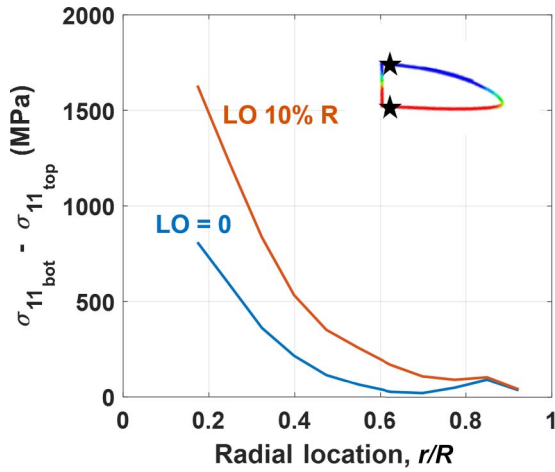
Fig. 15. Differential blade spar stresses (bottom - top) on upper rotor along the span for $LO = 0$ and $LO = 0.1$; $\mu = 0.1$.

Each part mesh is assigned three features: (1) blocks, (2) sidesets, and (3) nodesets. These are also generated in Cubit. They are used by the solver for important tasks. Blocks assign materials for flexible parts, sidesets identify aerodynamic surface nodes, and nodesets act as joint connections.

Aerodynamic model

The aerodynamic model is similar to any state-of-the-art beam-based comprehensive analysis—unsteady lifting line with airfoil decks and free-wake. The blade consists of a single airfoil—Boeing VR-7 with 2D C-81 properties extracted using in-house CFD calculations. The blade is swept back by $20°$ from $90\% R$. The root cutout is $10\% R$.

Rotor frequencies

The calculated rotor frequencies are shown in Fig. 9. At the nominal revolutions per minute (RPM) of 410, the frequencies clear all resonance crossings. The first flap frequency is at 1.44/rev, the first lag at 2.6/rev, and the first torsion at 8.6/rev. The first five frequencies are shown in Fig. 9.
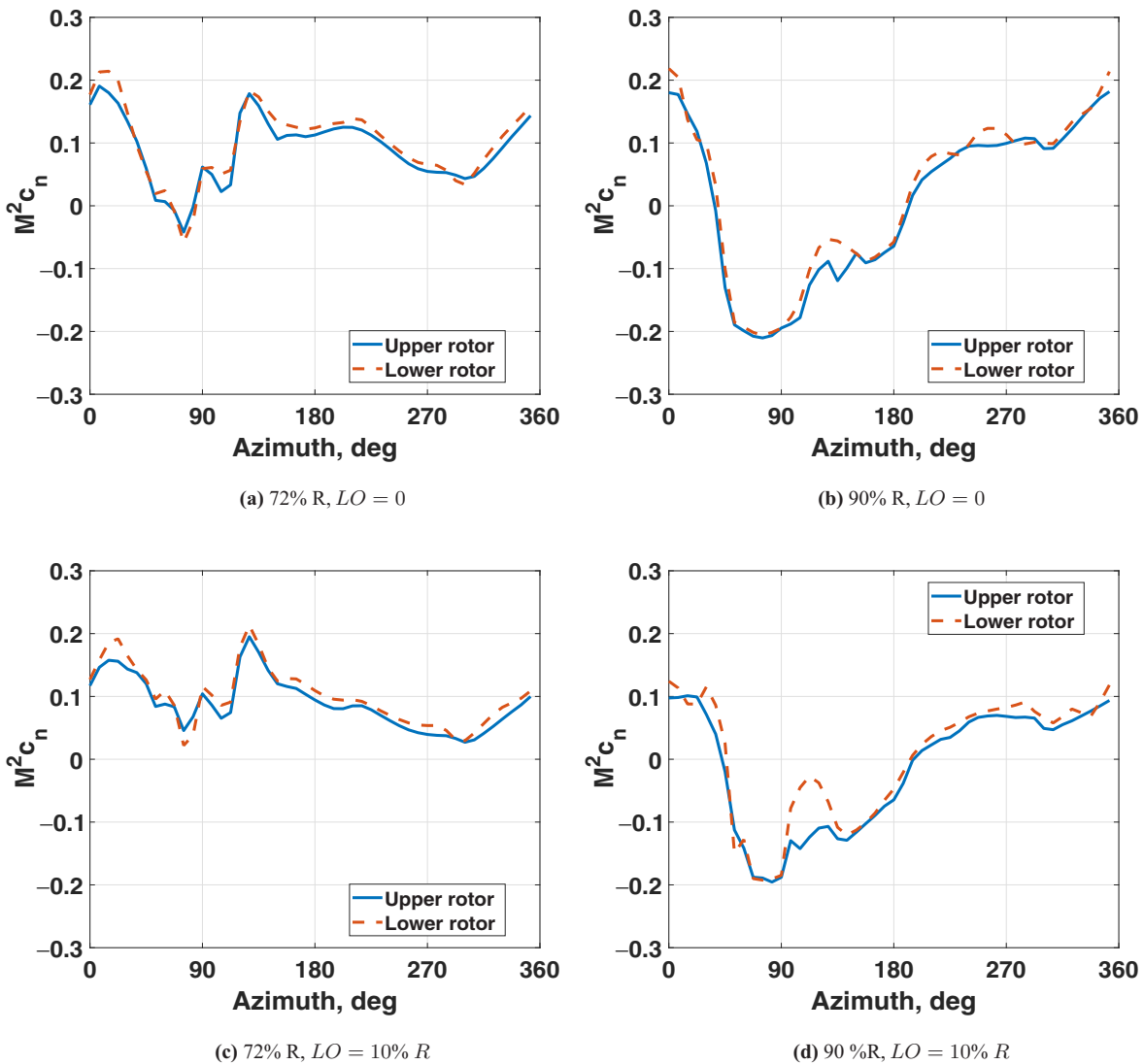

(a) 72% R, $LO = 0$

(b) 90% R, $LO = 0$

(c) 72% R, $LO = 10\% R$

(d) 90 %R, $LO = 10\% R$

Fig. 16. Predicted normal force versus azimuth at high speed, $\mu = 0.35$.

(a) 72% R, $LO = 0$

(b) 90% R, $LO = 0$

(c) 72% R, $LO = 10\%\ R$

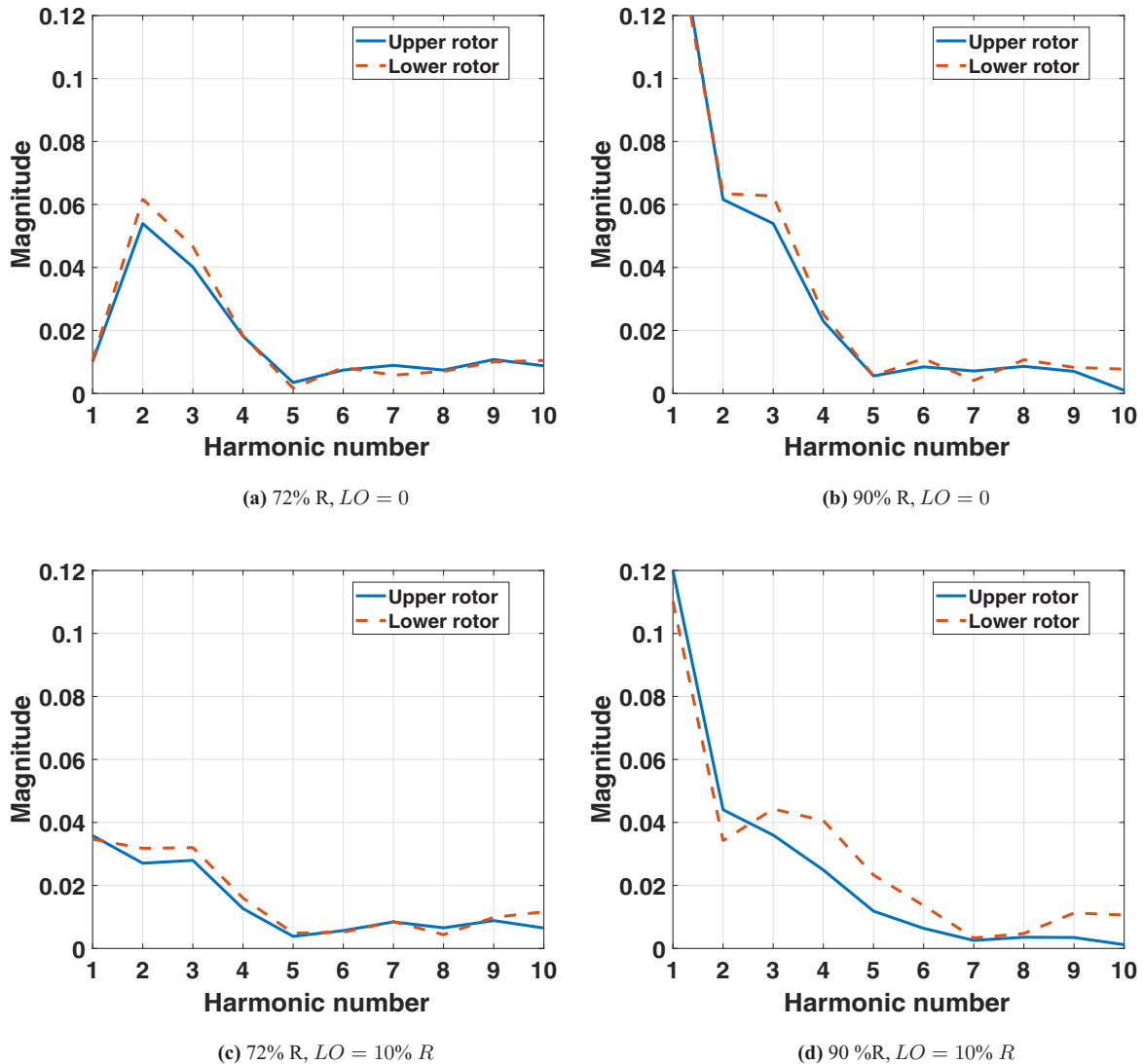**(d)** 90 %R, $LO = 10\%\ R$

Fig. 17. Predicted normal force harmonics at high speed, $\mu = 0.35$.

Trim model

A total of six trim controls are used. These are two collectives $\theta_{75}^U, \theta_{75}^L$; two longitudinal cyclics $\theta_{1s}^U, \theta_{1s}^L$; and two lateral cyclics $\theta_{1c}^U, \theta_{1c}^L$. The six trim targets are blade loading (C_T/σ), zero torque ($C_Q/\sigma = 0$), and individual hub roll and pitch moments (specified on the basis of lift-offset). Alternatively, five trim controls can be used. These are two collectives $\theta_{75}^U, \theta_{75}^L$; two longitudinal cyclics $\theta_{1s}^U, \theta_{1s}^L$; and one lateral cyclic $\theta_{1c}^U = \theta_{1c}^L$. The five trim targets would be blade loading, zero torque, net roll and pitch moments, and a lift-offset LO. The lift-offset is typically controlled via the longitudinal cyclics, hence this approach. Both approaches provide similar results, but the second was easier to achieve numerical convergence in trim for the nonzero LO case.

The periodic rotor solution was obtained using the modified harmonic balance algorithm (Ref. 2) with the rotor solution consisting of eight harmonics and executed on a hybrid distributed—shared memory architecture with 90 processors. The 6-degree-of-freedom trim solution for a coaxial rotor requires around 50 min of wall clock time. The free wake model is parallelized with shared memory OpenMP processors, with the number of processors equal to the number of tip trailers (eight in our case). The free wake computations for each trim iteration require 1 min

wall clock time for 10 wake turns and 20 revolutions in time with 7.5° azimuth step.

Low Speed

The low-speed transition flight is analyzed first to verify with results published recently by Sikorsky (Refs. 15, 16). The exact Sikorsky conditions for the low-speed flight regime were unavailable, except for the speed of 37 kt. Based on the rotor parameters, this corresponded to an advance ratio of $\mu = 0.1$. A forward shaft tilt of $\alpha = -2°$ is assumed, and a blade loading of $C_T/\sigma = 0.08$. The environment is Sea-Level/International Standard Atmosphere.

Airloads

The predicted blade normal force ($\approx$ lift) near the tip at 90%R is shown in Fig. 10 for two lift-offsets 0 and 0.1. The harmonic distributions are shown in Fig. 11. The 8/rev impulsive loading due to blade crossing is not very distinct but somewhat visible. The dominant vibratory loading is at 3–5/rev. These arise from the vortex-induced loading in the first and fourth quadrants similar to any conventional single main rotor helicopter.

The local azimuth of each rotor is used for comparing the airloads in Fig. 10 although they are rotating in opposite directions. The lower rotor has higher harmonics of 3–5 /rev. This is attributed to the upper wake impinging on the lower rotor. At low speed, this interaction is significant and can be observed as a magnified impulse in the first and fourth quadrants of the lower disk. Comparison of these predictions with the published S-97 airloads reproduced in Fig. 10(c) from Ref. 15 revealed that overall trends are similar. The S-97 results did not have axes labels, so the magnitudes could not be verified, but the relative magnitudes of the airloads were similar. Figure 12 shows the predicted wake geometry. The upper rotor wake hits the rear disk of the lower rotor—resulting in magnified impulses in the lower rotor airloads. The blade tips come quite closer on the retreating side of the upper rotor than on the advancing side.

Blade and hub stresses

Figs. 13(a) and 13(b) show the axial (bending) stresses (σ_{11}) for $LO = 0$ and 0.1, respectively. The blade skin is peeled off to visualize the internal stress concentration regions as the maximum bending stress is carried by the spar. Three observations are made. First, with $LO = 0.1$, the advancing blade produces more lift. As a result, the blades of the two rotors move away at $\psi = 90°$ but close in at $\psi = 270°$. This can be clearly seen in Fig. 14, which shows the rear view of blade motions. Second, the highest stresses occur near the advancing side of the disk. This is true for both lift-offset cases. Third, the stresses near the root increase with lift-offset as the bending moment increases significantly, which is as expected. Figure 15 shows the variation of spar stresses obtained as a difference between the bottom and top spar layers along the span. The differential stresses are due to flapwise bending. With $LO = 0.1$, the stresses almost double. It is also evident that the blade motion is predominantly characterized by the first flapping mode as the differential stress does not crossover the zero line. This behavior will change later at high speed. Finally, the distributions are evidently 3D in nature with localized patterns that vary from section to section.

High Speed

The conditions are the same as in low speed earlier; only the advance ratio is increased to $\mu = 0.35$. The actual aircraft will likely fly at a different shaft angle and reduce rotor tip speed. It is also likely to carry nonzero net hub pitch and roll moments to counter the effect of pusher prop and aircraft center of gravity travel and aerodynamic moments from fuselage and empennage. These are not included in the analysis in the absence of actual aircraft data.

Airloads

The effect of LO is crucial at high speed. First, consider zero LO.

The predicted blade normal force ($\approx$ lift) at two radial stations (72% R and 90% R) for $LO = 0$ is shown in Figs. 16(a) and 16(b), respectively. There is a significant negative lift near the tip, which is typical of an edgewise rotor with a high twist at this advance ratio. The phase of the maximum negative lift is around 80° or so, which is about 40–50° ahead of the UH-60 Black Hawk (Ref. 35). This is perhaps because there is little elastic torsion on these blades; the negative lift is mainly the effect of the longitudinal cyclic. So the vibratory loads are also expected to be lower. The harmonic breakdown is shown in Figs. 17(a) and 17(b), which confirms this expectation. The dominant harmonics are 2 and 3/rev. The cyclic and velocity vary as 1/rev across the disk. The lift is a function of cyclic and square of velocity which result in 2 and 3/rev variation. The 4 and 5/rev loadings are low. Concrete conclusions are premature without proper rotor properties and CFD-coupled pitching moments, but
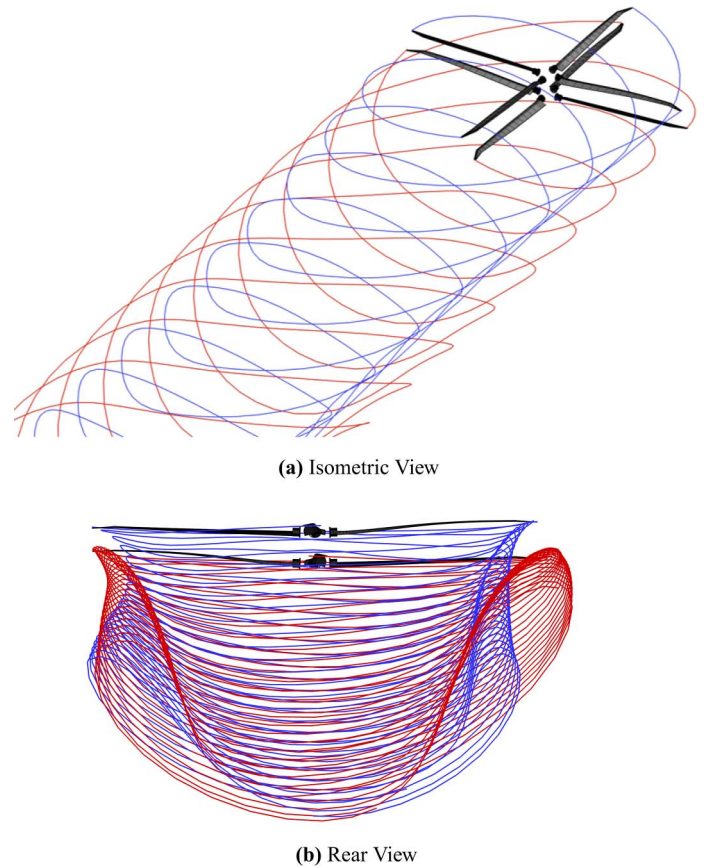

(a) Isometric View

(b) Rear View

Fig. 18. Free wake geometry at high speed; $\mu = 0.35$, $LO = 0.1$.

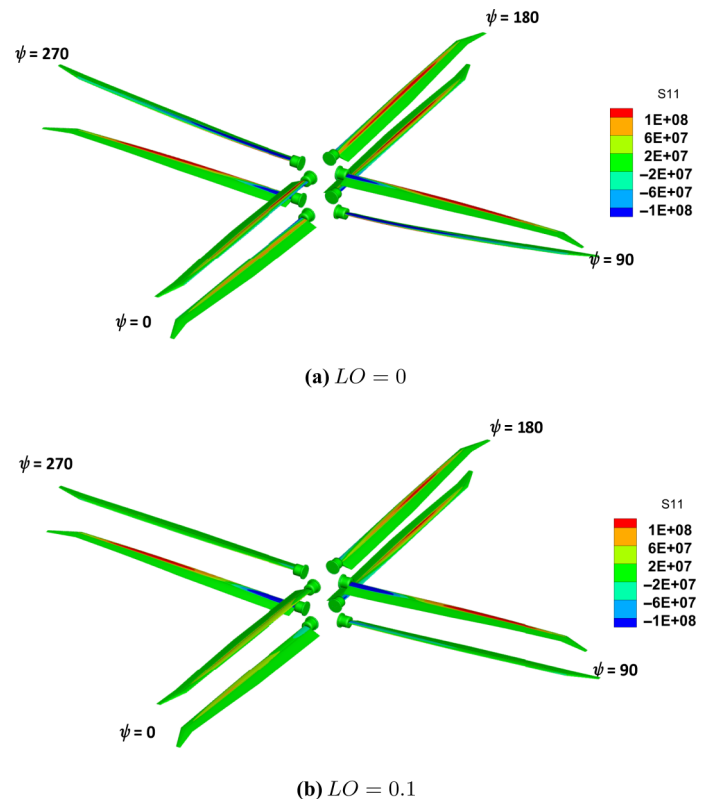**(a)** $LO = 0$

(b) $LO = 0.1$

Fig. 19. Axial stresses at high speed; $\mu = 0.35$, $C_T/\sigma = 0.08$, $\alpha_s = -2°$.
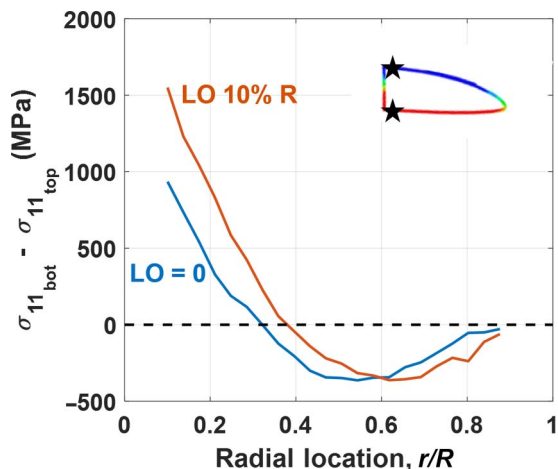
Fig. 20. Differential blade spar stresses (bottom - top) on upper rotor along the span for $LO = 0$ and $LO = 0.1$; $\mu = 0.35$.
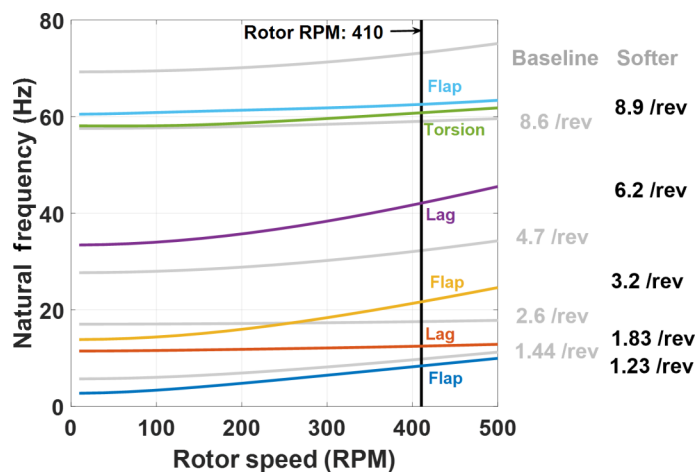

Fig. 21. Rotating frequencies for the softer Metaltail-II rotor blade; compared with the original model.

the predictions are self-consistent. It is also seen that the upper and lower rotors show similar harmonic content. This is expected as the wake is washed away, and the interactions between rotors become minimal.

Next, consider $LO = 0.1$.

The predicted blade normal force ($\approx$ lift) at the same two stations is shown in Figs. 16(c) and 16(d), respectively. The negative lift vanishes at the inboard station which is consistent with the lift increasing on the advancing side. The oscillatory loading is reduced by about 25% (from 0.4 to 0.3 peak to peak). The harmonic distribution is shown in Figs. 17(c) and 17(d). There is now greater 4 and 5/rev than before at the outboard station. The reason for this is not apparent. The airloads near the tip would benefit from RANS CFD analysis.

The wake interactions are less significant, as expected. Figure 18 shows the free wake geometry. The wake is washed away behind the rotor quickly, and very few interactions are evident between the upper and lower rotors near the blades.

Blade and hub stresses

Figures 19(a) and 19(b) show the axial (bending) stresses (σ_{11}) for $LO = 0$ and 0.1, respectively, with no blade skin. Three observations are made. First, without as expected, the stress concentration is clearly seen
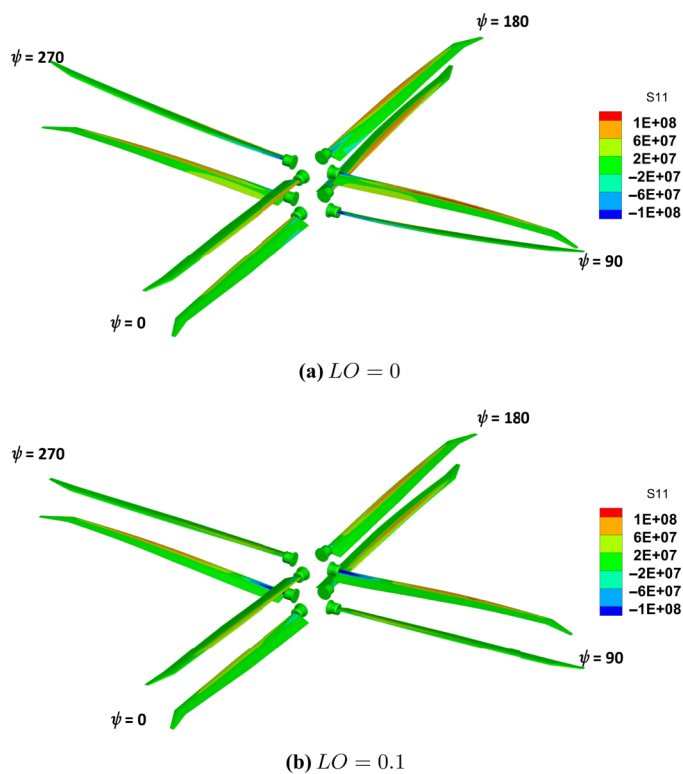

(a) $LO = 0$

(b) $LO = 0.1$

Fig. 22. Axial stresses at high speed with softer blade: $\mu = 0.35$, $C_T/\sigma = 0.08$, $\alpha_s = -2°$.
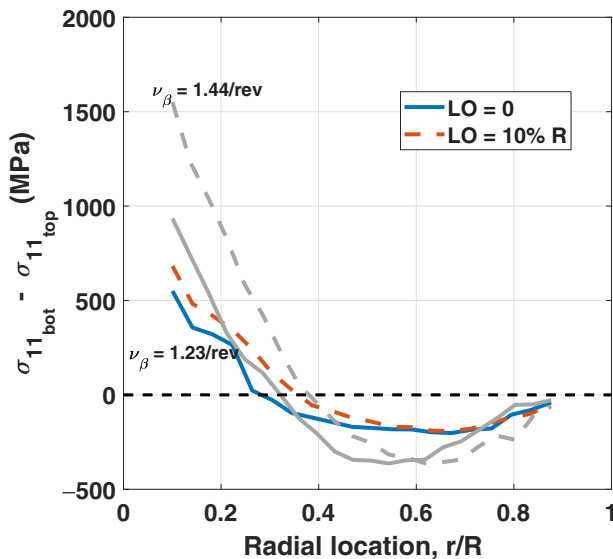

Fig. 23. Variation of differential blade spar stresses on upper rotor along the span for $LO = 0$ and $LO = 0.1$ to study the impact of blade flexibility; $\mu = 0.35$.

near the spar region. In each rotor, the highest stresses occur near the advancing side. Consider the blade at the advancing side of the upper rotor to study the effect of LO.

Figure 20 shows the variation of spar stresses obtained as a difference between the bottom and top spar layers along the span. With $LO = 0.1$, the stresses almost increase by 50% from $LO = 0$—which corresponds to a 25% rise in top and bottom layers. At high speed, the blade motion is
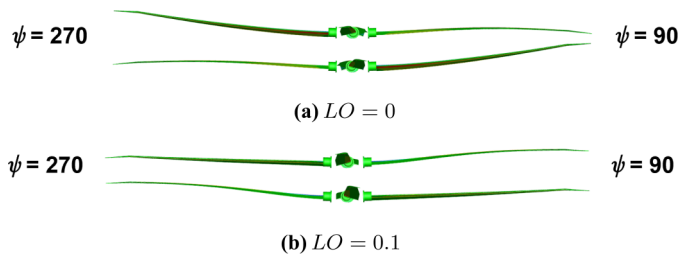
$\psi = 270$ $\psi = 90$

(a) $LO = 0$

$\psi = 270$ $\psi = 90$

(b) $LO = 0.1$

Fig. 24. Rear-side view of the coaxial rotor blades (softer) at high-speed flight with (a) $LO = 0$ and (b) $LO = 0.1$.

characterized by both first and second modes as the difference of stresses crosses the zero line. Towards midspan, the $LO = 0$ case has slightly higher stresses. This is because of the second bending mode, which is more dominant in the $LO = 0$ case—verified from Fig. 20 as the crossing of the zero line happens at an earlier radial station for the $LO = 0$ case.

In order to study the impact of greater blade flexibility on lower stresses, the root end design was changed to lower the first flap frequency. The 3D modeling provides parametric flexibility to implement such changes. The fanplot is shown in Fig. 21. The new first flap frequency is at 1.23/rev, the first lag at 1.83/rev, and the first torsion at 8.8/rev. The second flap which now appears at 3.16/rev is expected to have a significant impact.

Figures 22(a) and 22(b) show the axial (bending) stresses (σ_{11}) for $LO = 0$ and 0.1, respectively, with blade skin removed. Compared to the baseline (Fig. 19(b)), the retreating side now comes more closer to the blade strike with lift offset. Now consider the stresses. Figure 23 compares the differential stresses with the baseline. The stresses are dramatically reduced. The importance of the second mode is also evident from the crossover appearing further inboard. The maximum blade stresses near the root decrease by almost 100% with a softer blade—corresponding to a 50% drop in top and bottom flanges. The importance of the second mode to blade strikes is also clear from Fig. 24. The implication is that stresses can be relieved by lowering flap frequency if the second mode can be tailored to avoid blade strike.

Concrete conclusions are premature without higher fidelity aerodynamics and true hub data, but it is clear that 3D modeling can be used judiciously to extract deformation and stress information in an integrated manner.

Conclusions

A 3D solid FEA model was developed to predict blade and hub stresses of a lift-offset coaxial rotor. The model was built in CATIA, meshed in Cubit, and analyzed in X3D. The analysis coupled the 3D model with a lifting-line aerodynamic model. Two level flight regimes were considered: a low-speed transition flight ($\mu = 0.1$) and a high-speed cruise flight ($\mu = 0.35$). Two lift-offsets were considered: zero and 10% R. Two blade models were considered: baseline (flap frequency = 1.44/rev) and a softer blade (flap frequency = 1.23/rev). The stresses revealed interesting patterns in conjunction with deformations. Based on this work, the following key conclusions were drawn.

1) It is possible to predict the 3D stresses on a lift-offset coaxial rotor from the first principles. A toolchain consisting of CAD, 3D brick mesh generator CUBIT, and a scalable and parallel rotor aeroelastic solver X3D can accomplish this task effectively. The 6 degrees-of-freedom trim solution for a coaxial rotor requires around 50 min of wall clock time on 90 processors in a hybrid distributed—a shared memory architecture.

2) At low speed, the 3–5/rev vibratory airloads of the lower rotor were markedly higher. This behavior was consistent with the published S-97 prediction from Sikorsky.

3) At high speed, airloads showed no evidence of interrotor interactions. The wake geometry confirmed this behavior. So the vibratory harmonics of the upper and lower rotors were almost identical.

4) Analysis revealed interesting 3D stress patterns extending up to 50% R with significant concentrations inboard of 30% R.

5) At low speed, the differential blade spar stresses almost double along the span with lift-offset. The blade motion is predominantly characterized by the first flap mode.

6) At high speed, the differential blade spar stresses increase by 50% along the span with lift-offset. The blade motion is characterized by both the first and second flap modes. The second mode is more dominant with $LO = 0$ case resulting in higher midspan stresses.

7) Lift-offset stresses can be lowered (almost 50%) by lowering flap frequency as long as avoiding blade strike on the retreating side. The second mode is the dominant contributor and can be tailored to avoid the blade strike.

In future, the lifting-line model will be replaced with CFD, and the rotor hub refined to be more representative of an actual aircraft.

Acknowledgments

References

[1]Patil, M., and Datta, A., "Three-Dimensional Blade and Hub Stresses of Coaxial Rotors in High-Speed Forward Flight," AIAA 2023-1892, Proceedings of the AIAA SciTech Forum, National Harbor, MD, January 23–25, 2023.

[2]Patil, M., and Datta, A., "A Scalable Time—Parallel Solution of Periodic Rotor Dynamics in X3D," *Journal of the American Helicopter Society*, **66**, 042007 (2021), DOI: 4050/JAHS.66.042007.

[3]Datta, A., "X3D—A 3D Solid Finite Element Multibody Dynamic Analysis for Rotorcraft," Proceedings of the American Helicopter Society Technical Meeting on Aeromechanics Design for Vertical Lift, San Francisco, CA, January 20–22, 2016.

[4]Patil, M., and Datta, A., "Three-Dimensional Aeromechanical Analysis of Lift Offset Coaxial Rotors: A Helios Test Case," *Journal of Aircraft*, Vol. 61, (3), May 2024, pp. 939–956.

[5]Patil, M., and Datta, A., "Three-Dimensional Aeromechanical Analysis of Lift-Offset Coaxial Rotors," AIAA 2022-0928, Proceedings of the AIAA SciTech Forum, San Diego, CA, January 3–7, 2022.

[6]Patil, M., Arias, P., Baeder, J., and Datta, A., "An Integrated Three-Dimensional Aeromechanical Analysis of Lift-Offset Coaxial Rotors," Proceedings of the 78th Annual Forum of the Vertical Flight Society, Fort Worth, TX, May 10–12, 2022.

[7]Johnson, W., "Influence of Lift Offset on Rotorcraft Performance," NASA/TP-2009-215404, November 2009.

[8]Cheney, M. C., "The ABC Helicopter," Proceedings of the AIAA/AHS VTOL Research, Design and Operations Meeting, April 1969.

[9]Blackwell, R., and Millott, T., "Dynamics Design Characteristics of the Sikorsky X2 Technology Demonstrator Aircraft," Proceedings of the 64th Annual Forum of the American Helicopter Society, Montreal, Quebec, Canada, April 29–May 1, 2008.

[10]Bagai, A., "Aerodynamic Design of the X2 Technology Demonstrator Main Rotor Blade," Proceedings of the 64th Annual Forum of the American Helicopter Society, Montreal, Quebec, Canada, April 29–May 1, 2008.

[11]Walsh, D., Weiner, S., Arifian, K., Bagai, A., Lawrence, T., and Blackwell, R., "Development Testing of the Sikorsky X2 Technology Demonstrator," Proceedings of the 65th Annual Forum of the American Helicopter Society, Grapevine, TX, May 27–29, 2009.

[12]Walsh, D., Weiner, S., Arifian, K., Lawrence, T., Wilson, M., Millot, T., and Blackwell, R., "High Air-Speed Testing of the Sikorsky X2 Technology Demonstrator," Proceedings of the 67th Annual Forum of the American Helicopter Society, Virginia Beach, Virginia, May 3–5, 2011.

[13]Coleman, C. P., "A Survey of Theoretical and Experimental Coaxial Rotor Aerodynamic Research," NASA TP-3675, March 1997.

[14]Lorber, P., Law, G., O'Neill, J., Matalanis, C., and Bowles, P., "Overview of S-97 RAIDER Scale Model Tests," Proceedings of the 72nd Annual Forum of the American Helicopter Society, West Palm Beach, FL, May 17–19, 2016.

[15]Zhao, J., Brigley, M., and Modarres, R., "S-97 RAIDER Rotor Low Speed Vibratory Loads Analysis using CFD-CSD," AIAA 2019-0860, Proceedings of the AIAA SciTech Forum, San Diego, CA, January 7–11, 2019.

[16]Zhao, J., Xin, H., Modarres, R., and Brigley, M., "Methodology Correlation for Coaxial Rotor and Blade Load Prediction," Proceedings of the 76th Annual Forum of the Vertical Flight Society, Virtual, October 6–8, 2020.

[17]Johnson, W., Moodie, A. M., and Yeo, H., "Design and Performance of LiftOffset Rotorcraft for Short-Haul Missions," Proceedings of the American Helicopter Society Future Vertical Lift Aircraft Design Conference, San Francisco, CA, January 18–20, 2012.

[18]Yeo, H., and Johnson, W., "Investigation of Maximum Blade Loading Capability of Lift-Offset Rotors," Journal of the American Helicopter Society, 59, 012005 (2014), DOI: 4050/JAHS.59.012005.

[19]Lim, J., McAlister, K. W., and Johnson, W., "Hover Performance Correlation for Full-Scale and Model-Scale Coaxial Rotors," Journal of the American Helicopter Society, 54, 032005 (2009), DOI: 4050/JAHS.54.032005.

[20]Ramasamy, M., "Hover Performance Measurements Toward Understanding Aerodynamic Interference in Coaxial, Tandem, and Tilt Rotors," Journal of the American Helicopter Society, 60, 032005 (2015), DOI: 4050/JAHS.60.032005.

[21]Schmaus, J., and Chopra, I., "Aeromechanics of Rigid Coaxial Rotor Models for Wind-Tunnel Testing," Journal of Aircraft, Vol. 54, (4), August 2017, pp. 1486–1497.

[22]Klimchenko, V., and Baeder, J., "CFD/CSD Study of Interactional Aerodynamics of a Coaxial Compound Helicopter in High-Speed Forward Flight," AIAA 2020-0304, Proceedings of the AIAA SciTech Forum, Orlando, FL, January 6–10, 2020.

[23]Uehara, D., Sirohi, J., Feil, R., and Rauleder, J., "Performance of a Mach-Scale Coaxial Counter-Rotating Rotor in Hover," Journal of Aircraft, Vol. 53, (3), March 2016, pp. 746–755.

[24]Cameron, C., Karpatne, A., and Sirohi, J., "Blade Passage Loads and Deformation of a Coaxial Rotor System in Hover," Journal of Aircraft, Vol. 56, (6), December 2019, pp. 2144–2157.

[25]Jacobellis, G., and Gandhi, F., "Investigation of Performance, Loads, and Vibrations of a Coaxial Helicopter in High Speed-Flight," Proceedings of the 72nd Annual Forum of the American Helicopter Society, West Palm Beach, FL, May 17–19, 2016.

[26]Feil, R., Rauleder, J., Cameron, C., Karpatne, A., and Sirohi, J., "Aeromechanics Analysis of a High-Advance-Ratio Lift-Offset Coaxial Rotor System," Journal of Aircraft, Vol. 56, (1), January 2019, pp. 166–178.

[27]Singh, P., and Friedmann, P. P., "Aeromechanics and Aeroelastic Stability of Coaxial Rotors," Journal of Aircraft, Vol. 58, (6), August 2021, pp. 1386–1405.

[28]Johnson, W., and Datta, A.,"Requirements for Next Generation Comprehensive Analysis of Rotorcraft," Proceedings of the American Helicopter Society Specialist's Conference on Aeromechanics, San Francisco, CA, January 23–25, 2008.

[29]Lumba, R., and Datta, A., "Scalable mesh Partitioning for Multibody-3D Finite Element Based Rotary-Wing Structures," Computers and Structures, 281, 107015 (2023).

[30]Patil, M., and Datta, A., "Time-Parallel Trim Solution of Helicopter Rotors with Large-Scale 3D Structures," AIAA 2021-1079, Proceedings of the AIAA SciTech Forum, Virtual, January 11–15 and 19–21 2021.

[31]Staruk, W. J., Jayaraman, B., and Sitaraman, J., "Integrated 3D Structural Dynamics Using the Helios v9 Rotorcraft Analysis Framework," AIAA 2019-0842, Proceedings of the AIAA SciTech Forum, San Diego, CA, January 7–11, 2019.

[32]Wissink, A., Staruk, W., Tran, S., Roget, B., Jayaraman, B., Sitaraman, J., and Lakshminarayan, V., "Overview of New Capabilities in Helios Version 9.0," AIAA 2019-0839, Proceedings of the AIAA SciTech Forum, San Diego, 7–11 , January 7–11, 2019.

[33]Staruk, W., Datta, A., Chopra, I., and Jayaraman, B., "An Integrated Three-Dimensional Aeromechanics Analysis of the NASA Tilt Rotor Aeroacoustic Model," Journal of the American Helicopter Society, 63, 032002 (2018), DOI: 4050/JAHS.63.032002.

[34]Chi, C., Datta, A., and Panda, B., "Vacuum and Hover Tests of a Dihedral–Anhedral Tip Composite Rotor," Journal of Aircraft, Vol. 60, (5), September 2023, pp. 1700–1711.

[35]Datta, A., Nixon, M., and Chopra, I., "Review of Rotor Loads Prediction with the Emergence of Rotorcraft CFD," Journal of the American Helicopter Society, Vol. 52, (4), October 2007, pp. 287–317.